RSC Advances

PAPER

View Article Online
View Journal | View Issue

Cite this: *RSC Adv.*, 2019, **9**, 34457

Synthesis of a novel nano-rod-shaped hierarchical silicoaluminophosphate SAPO-11 molecular sieve with enhanced hydroisomerization of oleic acid to iso-alkanes†

Lingmei Yang,[abc] Huiwen Li,[abc] Jun ying Fu,[abc] Ming Li,[abc] Changlin Miao,[*abc] Zhongming Wang,[abc] Pengmei Lv[*abc] and Zhenhong Yuan[abc]

In this article, a novel nano-rod-shaped SAPO-11 molecular sieve (SAPO-11-A-F) with a thickness of *ca.* 100 nm was successfully fabricated by the *in situ* seed-induced steam-assisted method using the cationic surfactant cetyltrimethylammonium bromide (CTAB) as a mesoporous template and a nonionic copolymer poly(ethylene oxide)-*block*-poly(propylene oxide)-*block*-poly(ethylene oxide), F_{127}, as the crystal growth inhibitor. The fabricated nano-rod-shaped SAPO-11-A-F possessed nanocrystalline size, a hierarchical porous structure, and enhanced acidic sites. The added CTAB was mainly used to enhance the mesoporous structure and acid, and F_{127} acted as a grain growth inhibitor. According to the orientation growth mechanism of the molecular sieves, the crystallization mechanism of the nano-rod-shaped hierarchical porous molecular sieves with different crystallization times was investigated. It was found that the nano-rod-shaped molecular sieves were formed by the accumulation of nano-sheets. Compared to three nickel catalysts with different silicoaluminophosphate SAPO-11 molecular sieves in the hydroisomerization of oleic acid to iso-alkanes, the bifunctional catalyst of 7% Ni/SAPO-11-A-F had higher isomeric selectivity (79.8%); in particular, the isomeric octadecane showed stronger selectivity, indicating that the nano-rod-shaped SAPO-11 molecular sieve is more beneficial for the hydrodehydration reaction.

Received 6th August 2019
Accepted 2nd October 2019

DOI: 10.1039/c9ra06117g

rsc.li/rsc-advances

Introduction

The SAPO-11 molecular sieve has been widely used in the petrochemical industry.[1,2] The catalytic reaction performance is affected by the pore structure of the molecular sieve and the grain size.[3,4] The SAPO-11 molecular sieves are commonly synthesized by the hydrothermal method using a template agent.[5–7] It is easy to achieve self-aggregation for a high surface energy molecular sieve precursor (crystal nucleus) produced by crystallization at 160–200 °C. As a result, the grain size of the product is too large, generally 5–10 μm. To overcome the disadvantages such as the low apparent reaction rates of the reactants and products on molecular sieve catalysts, slow diffusion rates, low reaction selectivity, secondary cracking, and side reactions, nanometer molecular sieve catalysts have been studied recently.

Over the past decade, it has become increasingly recognized that generating nanozeolites is an effective route to enhance catalytic performances.[8,9] Venna *et al.*[10] successfully synthesized a nano-SAPO-34 molecular sieve with a high specific surface area using polyethylene glycol, polyoxyethylene lauryl ether, and methylene blue as polymerization inhibitors; nano-SAPO-34 synthesized with polyoxyethylene dodecyl ether showed a small grain size of 0.6–0.9 μm. Xiao's group[11,12] successfully synthesized a flake SAPO-11 molecular sieve with a thickness of 10–20 nm using di-*n*-propylamine as a microporous template and polyhexamethylene (PHMB) as a mesoporous template. The formation of nano-sheets was related to the gas composition produced by PHMB decomposition, and it was found that PHMB has a strong synergistic effect with microporous six-coordinated aluminum. The nano-sheet SAPO-11 exhibited good thermal stability compared to bulk SAPO-11. A Pt nanoparticle-modified nano-sheet (Pt/N-SAPO-11) catalyst exhibited higher isomerization selectivity and lower cracking of *n*-dodecane. Jin *et al.*[13] generated a hierarchically organized nano-SAPO-11 molecular sieve using a small-molecule growth inhibitor 1,2,3-hexanetriol and by altering the crystallization conditions. Meanwhile, it was found that the C–OH bonds within 1,2,3-hexanetriol can effectively cover the surface of the

[a]*Guangzhou Institute of Energy Conversion, Chinese Academy of Sciences, Guangzhou 510640, China. E-mail: miaocl@ms.giec.ac.cn; lvpm@ms.giec.ac.cn*
[b]*CAS Key Laboratory of Renewable Energy, Guangzhou 510640, China*
[c]*Guangdong Provincial Key Laboratory of New and Renewable Energy Research and Development, Guangzhou 510640, China*

† Electronic supplementary information (ESI) available. See DOI: 10.1039/c9ra06117g

embryonic crystal, inhibit its growth and regulate the grain size to form small particles. The small particles gradually grow from the shell to the core, eventually forming mesoporous small particles of nano-SAPO-11 molecular sieves. The hierarchical porous SAPO-11 molecular sieves catalyze *n*-heptane hydrogenation with high activity and isomeric selectivity. Recently, Bao's group[14] synthesized a button-shaped SAPO-11 molecular sieve with a size of around 1–1.5 μm, a hierarchical porous structure, and strong acidity by a two-step hydrothermal method using the cationic surfactant cetyltrimethylammonium bromide (CTAB) and a nonionic copolymer poly(ethylene oxide)-*block*-poly(propylene oxide)-*block*-poly(ethylene oxide), F_{127}; however, the fabricated SAPO-11 molecular sieves did not form nanoparticles. The 0.5% Pt/SAPO-11-H-catalyzed hydrogenation of *n*-octane exhibited high isomeric selectivity and low cleavage product selectivity. Moreover, the isomer selectivity of di-branched isomers increased, and the cracking selectivity is correspondingly weakened.

According to previous reports, the key factor in synthesizing nano-SAPO-11 molecular sieves is to control the gel concentration and crystal nucleus supersaturation. Chen *el al.*[2] designed a novel synthetic method of *in situ* inoculating seed-induced-SAC (SISAC) to fabricate silicoaluminophosphate SAPO-11 molecular sieves; the synthesis process involved low-temperature pre-crystallization, which could provide the maximum local concentration supersaturation and a large number of crystal nuclei to obtain smaller sized molecular sieves.[15] In the present study, novel nano-rod-shaped hierarchical porous SAPO-11 molecular sieves were synthesised through the *in situ* inoculating seed-induced-SAC method. In the synthesis process, the cationic surfactant cetyltrimethylammonium bromide (CTAB) and a crystal growth inhibitor, F_{127}, were added after the pre-crystallization of molecular sieves to form a nano-rod SAPO-11 molecular sieve structure. The physiochemical properties of the nano-rod molecular sieves, formation process, and crystallization mechanism of nano-rod-shaped SAPO-11 molecular sieves with hierarchical porous structures and their catalytic hydroisomerization performance for oleic acid were further investigated.

Experimental section

Synthesis of nano-hierarchical SAPO-11 molecular sieves

Tetraethyl orthosilicate (TEOS), aluminum isopropoxide (AIP), *ortho*-phosphoric acid (H_3PO_4), di-*n*-propylamine (DPA), CTAB, nickel nitrate hexahydrate, citric acid monohydrate, ethanol, and cyclohexane were obtained from Aladdin Chemical Reagent. The triblock copolymer mesoporous template (F_{127}, PEO_{106}-PPO_{70}-PEO_{106}, $M \approx 12\,600$, AR) was purchased from Macklin Chemical Reagent. The phosphoric acid (85% H_3PO_4) was obtained from the Sinopharm Chemical Reagent Company, P. R. China. The SAPO-11-C support was obtained from Nankai University Catalyst Co., Ltd. (China).

The typical gel ratio for SAPO-11 was $1.0Al_2O_3 : 1.0P_2O_5 : 0.3$TEOS $: 2.0$DPA $: 50H_2O$. For the initial gel, the SAPO-11 synthesis was carried out as follows: 13.62 g of AIP was dissolved in 30 mL of deionized water and stirred for 12 h. Then, 7.68 g of phosphoric acid was added to the aluminum isopropoxide solution and stirred for 4 h. Finally, 9.6 mL of di-*n*-propylamine and 2.6 mL of TEOS were slowly added and mechanically stirred for 6 h until they were mixed well.

The initial gel was pre-crystallized in an autoclave at 160 °C for 24 h (defined as DG-1). Certain amounts of CTAB and F_{127} (Al_2O_3 : CTAB : $0F_{127}$ = 1 : 0.03 : 0.0001) were dissolved in deionized water; then, the pre-crystallized sol was added to the micellar solution. The mixture was stirred and evaporated to dryness in a water bath at 60 °C. Then, 50 mL of absolute ethanol was added, and the mixture was continuously stirred and evaporated to dryness in a water bath at 60 °C. The residue was dried in a drying oven at 60 °C for 48 h to obtain a dry powder. Then, the dry powder was placed in a 20 mL crucible, and 20 mL of deionized water was added outside the crucible. The sol was crystallized at 200 °C for 24 h in a 100 mL crystallization vessel. Finally, the SAPO-11 molecular sieve, defined as SAPO-11-A-F, was collected by washing with water, dried in air, and calcinated at 600 °C with a heating rate of 2 °C min^{-1} for 10 h to remove the DPA, CTAB, and F_{127}. The SAPO-11 molecular sieve without added CTAB or F_{127} was denoted as SAPO-11-S; also, two samples, SAPO-11-A and SAPO-11-F, were fabricated through the same procedure used for synthesizing the SAPO-11 but without adding F_{127} and without adding CTAB, respectively.

Catalyst preparation

The SAPO-11 samples were loaded with 7 wt% nickel *via* a citric-acid-assisted impregnation method according to a literature report.[16] Nickel nitrate and citric acid were dissolved in 100 mL of absolute ethanol with a ratio of 1 : 1.5. The different SAPO-11 samples were loaded with 7 wt% Ni. The mixture was stirred in an oil bath at 60 °C for 4 h and then stirred at 80 °C for 12 h to obtain the dry powder precursor, which was then calcinated in air at 550 °C for 5 h. The reduction was carried out at 550 °C for 2 h under a 10% H_2/N_2 atmosphere to obtain a highly dispersed nano-7Ni/SAPO-11 catalyst.

Catalyst characterization

X-ray diffraction characterization was performed using an X'Pert Pro MPD X-ray diffractometer produced in the Netherlands (Cu Kα radiation source, $\lambda = 0.156$ nm, tube voltage of 40 kV, tube current of 40 mA, and scan range of 5 to 80°).

The specific surface areas and pore structures of the catalysts were tested using a Micromeritics ASAP Model 2020 automated physical adsorber (vacuum degassed at 300 °C for 10 h).

The microscopic morphologies of the catalyst surfaces were characterized using an S-4800 scanning electron microscope (SEM, Hitachi, Japan). The TEM tests were performed using a JEOL JEM-2100F field-emission transmission electron microscope with an instrument acceleration voltage of 200 kV.

The hydrogen temperature-programmed reduction (H_2-TPR) was tested using a Micromeritics AutoChem 2950 HP instrument using a thermal conductivity detector.

The acidities and acid amounts of the catalysts were measured using NH_3-TPD (model: Autosorb-iQ-C). First, the impurity gas

present in the sample was removed by heating at 500 °C with helium as the carrier gas, and ammonia absorption was saturated at 100 °C. Then, the temperature was increased from room temperature to 800 °C at a rate of 10 °C min^{-1}.

The acid types of the catalysts were detected using a pyridine-infrared spectrometer (model: Nicolet 6700). The sample was first evacuated to 10^{-2} Pa at 200 °C and was then exposed to pyridine for 15 min at room temperature, followed by degassing at 200 °C and 350 °C for 1 h.

^{29}Si and ^{27}Al nuclear magnetic resonance measurements (MAS NMR) were performed on a Bruker Ascend-500 solid-state nuclear magnetic instrument (Germany) using a 4 mm three-resonance nuclear magnetic probe with a sample rotation speed of 15 kHz.

Catalytic tests

The hydroisomerization of oleic acid was conducted in a high-pressure autoclave with 0.7 g of catalyst. The experiment was maintained for 4 h at a temperature of 360 °C under 4 MPa H_2 pressure. The outgas products were collected in a 0.5 L airbag, and the liquid products were filtered through a 0.22 μm organic membrane. The liquid product was diluted with 1 : 100 cyclohexane. The liquid product was qualitatively analyzed using a cracker-gas chromatography-mass spectrometer (Agilent 7890A-5975C) equipped with an HP-5 capillary column with dimensions of 30 m × 0.25 mm × 0.25 μm.

Results and discussion

Physicochemical properties of nano-rod-shaped SAPO-11 molecular sieves

The SEM and TEM images of the different SAPO-11 samples synthesized by the SISAC method are shown in Fig. 1. From Fig. 1, the low-magnification SEM image (Fig. 1A) shows that the SAPO-11-S molecular sieve exhibited a spherical structure with a relatively smooth surface, and the primary grain size was 2 to 3 μm; no small grains were scattered outside the crystal, indicating that no irregular amorphous phase structure was present. The low-magnification SEM image (Fig. 1B) reveals that the SAPO-11-A molecular sieve consisted of sea urchin SAPO-11 with a size of 1 to 2 μm. The TEM image (Fig. S1†) reveals that the SAPO-11-A sample is assembled from nano-rods with a thickness of about 20 nm. The SEM image (Fig. 1C) confirms that a nano-rod-like SAPO-11-A-F molecular sieve was formed by adding the CTAB and F_{127}. Further, the TEM image in Fig. 1D shows a nano-rod-like SAPO-11 molecular sieve with a length of 500 nm and a width of about 100 to 200 nm. According to literature reports, the triblock copolymer F_{127} acts as a polymerization inhibitor in the synthesis of molecular sieves to generate nano-sized grains.[17,18] In addition, the corresponding elemental mappings of O, Al, P, and Si for the SAPO-11-A-F molecular sieve confirm the uniform distribution of all elements.

The XRD patterns of the different SAPO-11 samples are plotted in Fig. 2. All the molecular sieves exhibited the corresponding diffraction peaks at $2\theta = 8.1$, 9.4, 13.1, 15.6, 20.3, 21.2, and 22.1 to 23.2°. This can be attributed to the AEL structure of the SAPO-11 molecular sieve. These results indicate that the addition of the surfactant CTAB and triblock copolymer F_{127} did not change the crystal structure of the molecular sieve. However, the addition of CTAB and F_{127} broadened the diffraction peak of the molecular sieve, indicating decreased crystallinity and particle size of the SAPO-11 molecular sieve. The relative crystallinities of the different SAPO-11 molecular sieves are shown in Table 1. The relative crystallinity of the SAPO-11-A molecular sieve is 98.1%, and the SAPO-11-F sample is only 62.8% that of SAPO-11-S. Meanwhile, the relative crystallinity of the SAPO-11-A-F molecular sieve is 85.3% that of SAPO-11-S; this indicates that during the crystallization processing of the molecular sieve, the addition of CTAB surfactant and F_{127} jointly affected the crystallization of the molecular sieve, thus forming the nano-rod-shaped hierarchical SAPO-11-A-F molecular sieve.

The surface areas, pore volumes, and the relative crystallinities of the four SAPO-11 molecular sieve samples prepared by

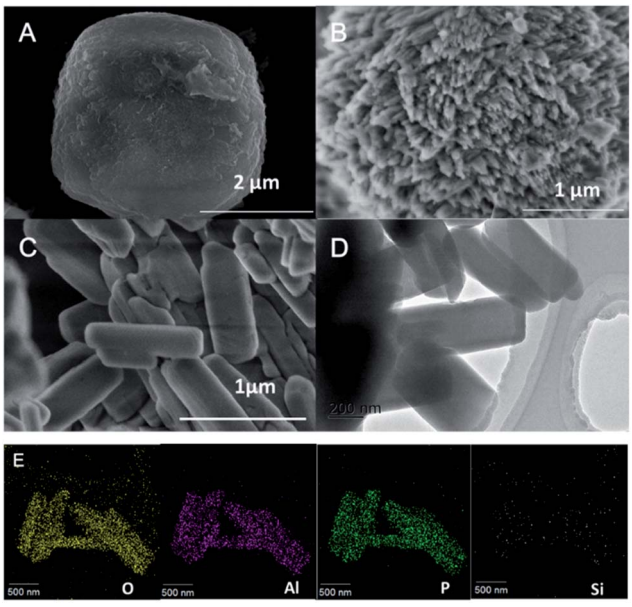

Fig. 1 The SEM and TEM images of SAPO-11-S (A), SAPO-11-A (B), SAPO-11-A-F (C and D); the elemental mapping of SAPO-11-A-F (E).

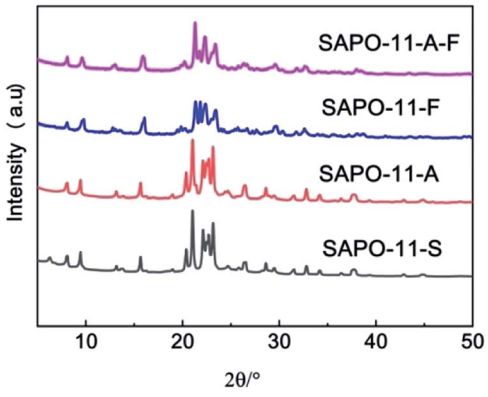

Fig. 2 XRD patterns of the different SAPO-11 samples.

Table 1 The results of the surface area, pore volume and relative crystallinity (RC) of the different SAPO-11 samples

Catalysts	S_{BET}[a] ($m^2\ g^{-1}$)	S_{mic}[b] ($m^2\ g^{-1}$)	S_{ext} ($m^2\ g^{-1}$)	V_{meso}[c] ($cm^3\ g^{-1}$)	V_{mic} ($cm^3\ g^{-1}$)	V_{toal} ($cm^3\ g^{-1}$)	R (%)
SAPO-11-S	217.9	107.5	110.4	0.153	0.046	0.232	100
SAPO-11-A	283.9	133.2	150.8	0.203	0.057	0.260	98.1
SAPO-11-F	257.6	202.9	54.7	0.117	0.082	0.210	62.8
SAPO-11-A-F	249.3	123.7	125.6	0.172	0.051	0.241	85.3

[a] Surface area calculated by the BET method. [b] Micropore volume and surface area calculated by the *t*-plot method. [c] Mesopore volume calculated by the BJH method.

the *in situ* seed-induced steam-assisted method are shown in Table 1. SAPO-11-A has a significantly larger external surface area (150.8 $m^2\ g^{-1}$) than SAPO-11-S (110.4 $m^2\ g^{-1}$), as shown in Table 1. Meanwhile, the pore volumes showed that the mesoporous volume increased with the addition of CTAB cationic surfactant. SAPO-11-F shows an increased micropore surface area compared with SAPO-11-S (202.9 $m^2\ g^{-1}$ *vs.* 107.5 $m^2\ g^{-1}$). This is because the macromolecular structure of F_{127} can inhibit the growth of crystals and form more microporous structures. With the simultaneous addition of CTAB and F_{127}, SAPO-11-A-F exhibited an increased surface area (249.3 $m^2\ g^{-1}$) and mesoporous volume (0.172 $cm^3\ g^{-1}$) compared with SAPO-11-S; this indicates that the coexistence of the surfactant CTAB and polymerization inhibitor F_{127} affected the formation of SAPO-11-A-F molecular sieve pores and cages during molecular sieve formation through the *in situ* seed induction steam-assisted method.

The adsorption and desorption of N_2 and pore size distribution curves of the different SAPO-11 samples are displayed in Fig. 3a. It can be seen that the SAPO-11 molecular sieves present typical H1-type adsorption and desorption, and the IV type annular hysteresis loop generated by mesoporous capillary coagulation occurred at a relative pressure of $P/P_0 = 0.4$ to 1.0.[19,20] The four SAPO-11 molecular sieves exhibited mesoporous structures at relative pressures of $P/P_0 = 0.4$ to 0.5 and $P/P_0 = 0.8$ to 0.95.[21] According to the NLDFT results, Fig. 3b shows the corresponding pore size distribution curves of the different SAPO-11 molecular sieves. All the SAPO-11 molecular sieves had micro-mesopore structures. The SAPO-11-S pore size distribution (adsorption branch) at *ca.* 3.7 nm can be observed in Fig. 3b; the most accessible pore sizes of SAPO-11-A-F were 1.1 nm and 3.9 nm. This is mainly because the triblock copolymer F_{127} has a large molecular weight and contains hydrophobic and hydrophilic groups, which inhibit crystal growth.

Fig. 4 shows the acidic properties of the Brønsted (B) and Lewis (L) acid sites for the different SAPO-11 samples determined by Py-IR. The bands at *ca.* 1450 cm^{-1}, 1545 cm^{-1}, and approximately 1490 cm^{-1} correspond to pyridine molecules adsorbed on L acid sites and B acid sites and the coefficient peak of B and L acidic sites, respectively.[22–24] Table 2 shows the calculated results of B acid, L acid, and medium-strong acid sites absorbed-desorbed by pyridine molecules at 200 °C and 350 °C, respectively. Compared with SAPO-11-S, the amounts of B acid, L acid, and total acid of SAPO-11-A-F were increased significantly by adding CTAB and F_{127} to the synthesis system; when the desorption of pyridine proceeded at 350 °C, the SAPO-11-A-F sample contained strong B and L acidic sites, and the total acid amount reached 194 μmol g^{-1}. Meanwhile, for SAPO-11-F with the addition of F_{127} alone, only the amount of B acid sites increased.

The NH_3-TPD profiles of different SAPO-11 samples are shown in Fig S2.† The acidic properties have been listed in Table S1.† The SAPO-11 samples showed two profiles at approximately 210 °C and 350 °C, attributable to weak and medium-strong acid sites in the samples, respectively. Compared with SAPO-11-S, the acid site content of SAPO-11-F decreased, while the acid sites of SAPO-11-A-F slightly increased; especially, the area of the high-temperature peak increased, indicating that the added surfactants CTAB and F_{127}

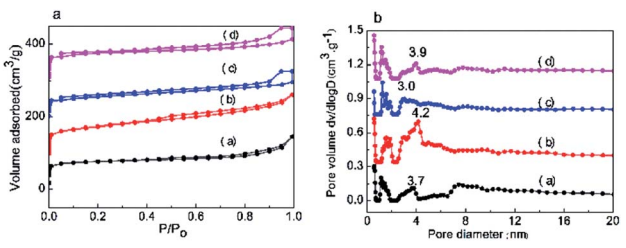

Fig. 3 (a) N_2 adsorption–desorption and (b) pore size distributions of the different SAPO-11 samples: (a) SAPO-11-S, (b) SAPO-11-A, (c) SAPO-11-F and (d) SAPO-11-A-F.

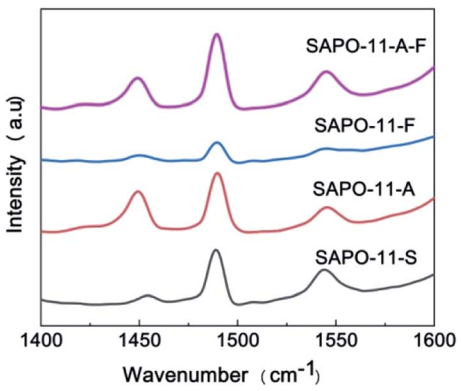

Fig. 4 IR spectra of pyridine adsorption for the different SAPO-11 samples at 200 °C.

Table 2 Acidity properties of the SAPO-11 samples determined by Py-IR

	Amount (μmol g^{-1}) and distribution of acid sites					
	Total acid sites (200 °C)			Medium and strong acid sites (350 °C)		
Sample	B	L	B + L	B	L	B + L
SAPO-11-S	144	22	166	122	18	140
SAPO-11-A	175	100	275	140	31	171
SAPO-11-F	181	20	201	149	17	166
SAPO-11-A-F	188	110	298	153	41	194

enhanced the acidity of the molecular sieve, which is consistent with the Py-IR results.

Fig. 5 shows the ^{29}Si MAS NMR spectra examining the local environments of the Si atoms in two molecular sieve samples, SAPO-11-S and SAPO-11-A-F. The ^{29}Si NMR spectra of the two SAPO-11 samples show a broad band in the range of −80 to −120 ppm. The resonance peaks at −88 ppm, −97 ppm, −103 ppm, −108 ppm and −112 ppm correspond to Si(4Al), Si(3Al), Si(2Al) Si(1Al) and Si(4Si) environments, respectively.[25,26] The Si(4Al) species involves replacing a P atom with a Si atom to form a Si(4Al) site by an SM2 mechanism, forming a weak Brønsted acid site.[27] The Si($4-n$Al) ($0<n<4$) species accords Si at the SAPO boundary by a synergistic SM2 and SM3 mechanism, which is essentially a medium-strong Brønsted acid site, and the Si(4Si) species represents Si islands. The ^{29}Si NMR spectrum of SAPO-11-A-F has a smaller peak area at −112 ppm than SAPO-11-S, indicating fewer Si islands and a different Si environment. From Table 3, the SAPO-11-A-F sample has a higher content of Si ($4-n$Al) ($0<n<4$) species, but less Si(4Si) than SAPO-11-S; this indicates that SAPO-11-A-F contains more weak and strong acid sites, which should be favourable for hydroisomerization reactions. The ^{29}Si NMR spectral analysis is consistent with the Py-IR and NH_3-TPD results.

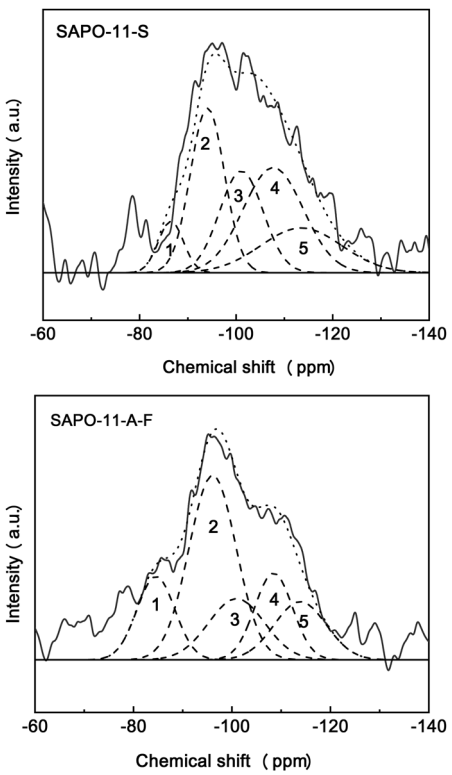

Fig. 5 ^{29}Si MAS NMR spectra of the SAPO-11-S and SAPO-11-A-F species.

As displayed in Fig. 6, the ^{27}Al solid state NMR spectrum of SAPO-11-A-F exhibits a main peak at 37 ppm and a smaller peak at 33 ppm, while the SAPO-11-S spectrum contains only the main peak at 37 ppm; this is due to a tetrahedrally coordinated aluminum ion bound *via* oxygen to four P atoms,[3] which represents most of the tetrahedrally coordinated aluminum ions that enter the pore structures.

Crystallization mechanism of the nano-rod-shaped SAPO-11 molecular sieve

To obtain a clear understanding of the structural evolution and formation mechanism of the nano-rod hierarchical SAPO-11-A-F molecular sieve, powder XRD patterns (Fig 4S†) were used to characterize the pre-crystallization power (DG-1) to analyse the crystal growth route of nano-rod SAPO-11-A-F. It can be seen that DG-1 has an amorphous phase with a very high peak at $2\theta = 6.2^\circ$, and it is a long-chain-ordered layered intermediate, forming a (100) layered semicrystalline structure;[28,29] this probably formed *via* van der Waals forces or very weak hydrogen bonding in the pre-crystallization process.[29]. The XRD patterns of the SAPO-11 samples at a pre-crystallization time of 24 h at 160 °C exhibit some emerging characteristic peaks corresponding to the AEL structure, indicating that the AEL structure initially formed. In the SEM image (Fig S5†), numerous nanocrystalline particles can be seen; this indicates that after the pre-crystallization, the silicate, aluminate, and phosphate species pre-crystallized to form nano-crystal particles.

The XRD spectra and the relative crystallinity curves of SAPO-11-A-F at different crystallization times are shown in Fig. 7 and S6.† When the crystallization time reached 1 h, the XRD pattern showed a reflection peak with $2\theta = 6.2^\circ$, which corresponds to the (100) layered intermediate structure.[28,29] Meanwhile, the XRD spectra show some weak diffraction peaks at $2\theta = 8.1$, 21.2, and 22.1 to 23.2°, which were attributed to the AEL structure of the SAPO-11 molecular sieve. When the crystallization time was extended to 3 hours, the diffraction peak at $2\theta = 6.2^\circ$ weakened, while the AEL diffraction peaks corresponding to $2\theta = 8.1$, 9.4, 13.1, 15.6, 20.3, 21.2 and 22.1 to 23.2° increased, indicating that

Table 3 Deconvolution results of the ^{29}Si MAS NMR spectra of SAPO-11-S and SAPO-11-A-F *via* the peak areas of the different Si species

Sample	Si(4Al)%	Si(3Al)%	Si(2Al)%	Si(1Al)%	Si(4Si)%
SAPO-11-S	6.1	26.4	20.7	29.6	16.9
SAPO-11-A-F	17.4	37.9	18.7	18.1	7.9

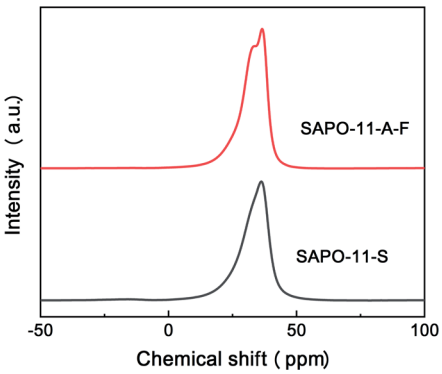

Fig. 6 ^{27}Al MAS NMR spectra of SAPO-11-S and SAPO-11-A-F.

the solid sample mainly contains coexisting layered intermediate structures and AEL structures; at the same time, the relative crystallinity of SAPO-11-A-F reached 47.5% (Fig. S3†). As the crystallization time reached 6 h, the diffraction peak at $2\theta = 6.2^\circ$ disappeared completely, and the sample fully displayed the diffraction peak of AEL crystal phase. The relative crystallinity reached 73%. When the crystallization time was 12 h, the relative crystallinity reached 95%.

To elucidate the formation process, nano-rod SAPO-11-A-F with different crystallinity times was characterized by SEM (Fig. 8). When amounts of CTAB and F_{127} were added to the dry-gel, nano-sheets with lengths *ca.* 500 nm were observed. While the dry-gel was further crystallized for 1 h at 200 °C, the sheet-like thin layers were connected between the layered intermediates, in which the XRD spectra showed the amorphous phase. After 3 h, large nano-rod-shaped particle aggregates were present, and the surface showed small crystals, conforming to the dissolution of small crystals; these grew further into larger crystals by the mechanism of Ostwald ripening. [30,31] After 8 h of crystallization, nano-rod-shaped structures were observed. As the crystallinity time was further prolonged to 12 h, the surface showed irregular nano-rods. When the time was increased to 24 h, the surface of the nano-rods was smoother and more uniform. According to the SEM tests, we can see that nano-rod SAPO-11 was grown from the nano-sheet-like structures.

According to the non-classical molecular sieve orientation growth mechanism, the proposed mechanism of nano-rod-shaped multistage pore crystallization is shown in Fig. 9: (1) First, silicate, aluminate, and phosphate are pre-crystallized to form nano-crystal particles. (2) The added cationic surfactant CTAB and triblock copolymer F_{127} also enter the interlayer, and secondary nucleation occurs between the two surfactants and polysilicate, aluminate, and phosphate. F_{127} inhibits grain growth in the nucleus, decreases agglomeration between ions, and forms nano-crystals. (3) The nano-crystals form a nano-sheet structure according to the orientation aggregation, and the nano-sheet structure undergoes intragranular curing. The adjacent nanoparticles in the nano-sheets are fused to form nano-rod structures. The single-crystal structure and particle size remain unchanged.

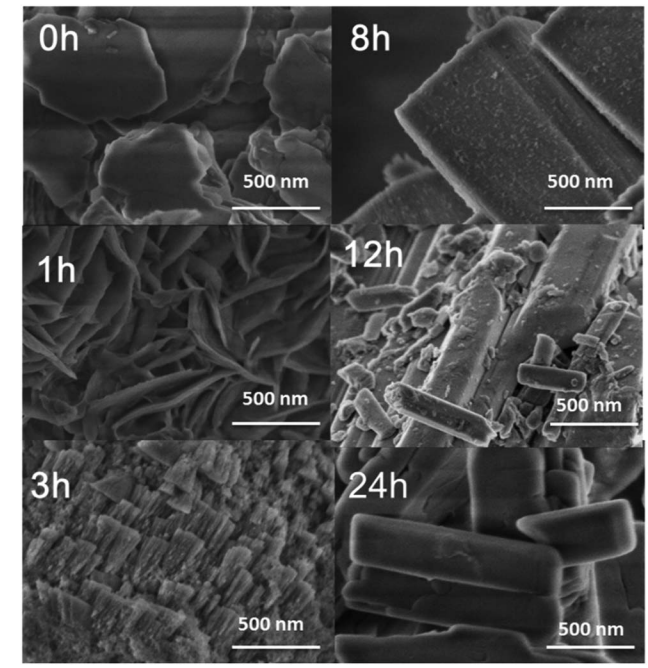

Fig. 8 SEM images of SAPO-11-A-F with different crystallization times.

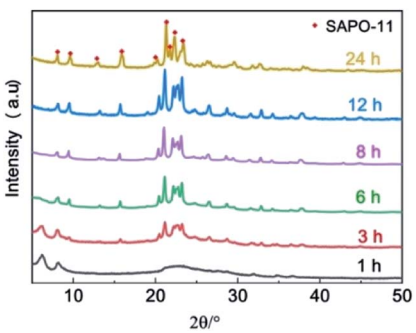

Fig. 7 XRD spectra of SAPO-11-A-F with different lengths of crystallization time (1, 3, 6, 8, 12 and 24 h).

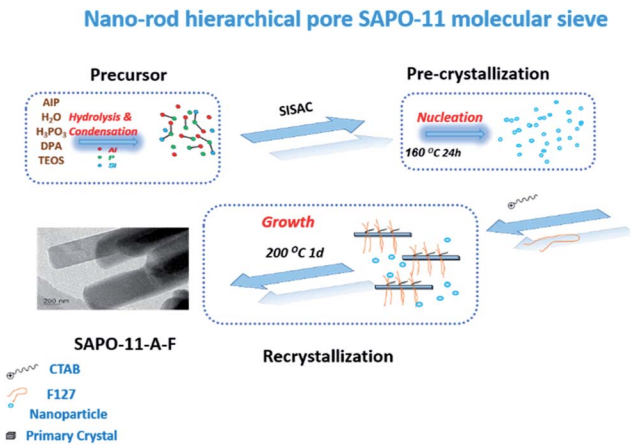

Fig. 9 Schematic of the proposed SAPO-11 crystal growth route by the SISAC method.

Catalytic performance for hydroisomerization of oleic acid

The SAPO-11-S and SAPO-11-A-F molecular sieves supported loading of 7 wt% nickel catalyst *via* a citric-acid-assisted impregnation method. The TEM images of the different Ni/SAPO-11 samples are displayed in Fig. S6.† It was found that the nickel nanoparticles were well distributed on the different SAPO-11 supports, and the nickel nanoparticle size was about 10 nm; which is larger than the SAPO-11 microporous channels (2 to 4 nm). Furthermore, the H_2-TPR profiles of the 7Ni/SAPO-11-S and 7Ni/SAPO-11-A-F species displayed catalytic reduction performance (Fig. 10). The two catalysts have two reduction peaks; the first peak is around 380 °C, which is assigned to the reduction of bulk NiO, and the second hydrogenation consumption peak is around 470 °C, which is assigned to the reduction of NiO species which have strong interactions with SAPO-11.[32] The peak areas of the higher-temperature reduction peaks for the 7Ni/SAPO-11-A-F catalyst were smaller than those for the 7Ni/SAPO-11-S catalyst, indicating that nano-rod hierarchical SAPO-11 has weak interactions with nickel particles and that the catalysts could be readily reduced.

Hydrogenation reaction of oleic acid was selected as the model reaction to study the catalytic performance of three different catalysts (7Ni/SAPO-11-C, 7Ni/SAPO-11-S and 7Ni/SAPO-11-A-F). The conversions and selectivities of the liquid product compositions and C_{iso}/C_n of oleic acid hydroisomerization over the different 7Ni/SAPO-11 catalysts are shown in Fig. 11. Notably, the conversion of oleic acid was 100% in the hydrogenation reaction over the 7Ni/SAPO-11 catalyst at a reaction temperature of 360 °C, a reaction time of 4.0 h, and a H_2 pressure of 4 MPa. Combining these experiments, the liquid products were mainly *n*-C_{17}, *n*-C_{18}, iso-C_{17}, iso-C_{18}, and a small amount of C_8–C_{16} alkanes. Compared with 7Ni/SAPO-11-C catalyst, the isomeric selectivity of oleic acid of 7Ni/SAPO-11-A-F increased from 64.2% to 78.9%, and its C_{iso}/C_n ratio increased from 1.67 to 3.73. Especially, was is found that the selectivity of hetero-octadecane was increased significantly by the 7Ni/SAPO-11-A-F catalyst, and heterogeneous heptadecane decreased accordingly; this indicates that the nano-rod SAPO-11 molecular sieve was more beneficial for producing octadecane by a hydrodehydration reaction.

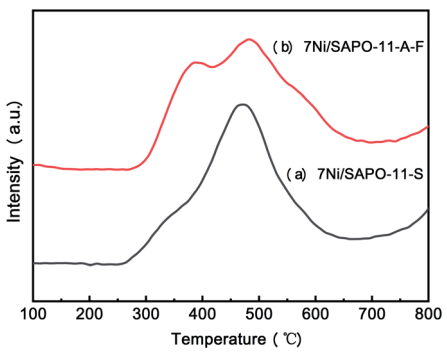

Fig. 10 H_2-TPR profiles of (a) 7Ni/SAPO-11-S and (b) 7Ni/SAPO-11-A-F.

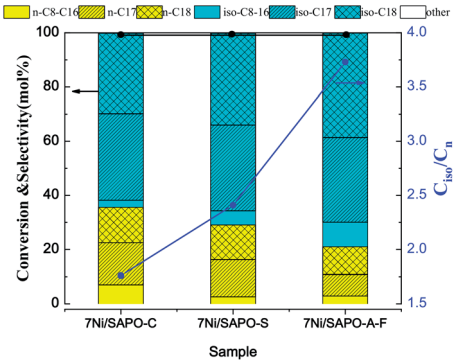

Fig. 11 The conversion and selectivity of the liquid product compositions and C_{iso}/C_n of oleic acid hydroisomerization over different 7Ni/SAPO-11 catalysts (reaction conditions: oleic acid (15 g), catalyst (0.7 g), $T = 360$ °C, $t = 4.0$ h, $P = 4$ MPa H_2).

Conclusions

In summary, a novel nanorod-shaped hierarchical porous SAPO-11 molecular sieve was synthesized by the *in situ* seed-assisted steam method with the cationic surfactant CTAB and triblock copolymer F_{127}. The physiochemical properties of the nano hierarchical molecular sieves were investigated by a series of characterization analyses, which indicated that the molecular sieves maintained AEL structures irrespective of the addition of mesoporous template CTAB and triblock copolymer F_{127}, and its relative crystallinity decreased. A hierarchical porous structure was formed by adding triblock copolymer F_{127} and mesoporous template CTAB (average pore sizes of 1.1 and 3.9 nm). In particular, the structure of the molecular sieve changed significantly from an ellipsoid structure to a nano-rod structure. By comparison with a sample fabricated with the mesoporous template agent CTAB alone and a sample fabricated with the triblock copolymer F_{127} molecular sieve alone, it was found that the role of the mesoporous template agent CTAB was to produce mesopores and enhance the acidity during the synthesis of the molecular sieves, while F_{127} acted as a grain growth inhibitor to control the grain size.

The crystallization mechanism of the SAPO-11-A-F molecular sieve was analysed by characterizing samples with different crystallization times and the orientation growth mechanism of the molecular sieve. Silicate, aluminate, and phosphate were first pre-crystallized to form a nanocrystalline nucleus. Then, nanocrystals were obtained by the renucleation of added CTAB and F_{127} in the interlayer structure with silicate, aluminate, and phosphate. The nanograins aggregated and formed a nanosheet structure according to the orientation, and the nanosheet structure was subjected to intragranular curing. The adjacent nanoparticles merged, and the nanosheets gradually grew to form nanorod structures. 7Ni/SAPO-11-A-F had different effects on the hydroisomerization of oleic acid because of its nano-hierarchical porous structure; especially, the selectivity of iso-octadecane was higher than that of isomeric heptadecane.

Conflicts of interest

There are no conflicts to declare.

Acknowledgements

The financial support received from the National Natural Science Foundation of China (No. 51806225, No. 21576260 and No. 51606201), Guangdong Special Support program (2017TX04Z109), Natural Science Foundation of Guangdong Province (No. 2018A030310078), National Key Research and Development Plan (No. 2017YFD0601003) and Guangzhou Science and Technology Plan Project (No. 201804010125) is much appreciated.

Notes and references

1 G. Xing, S. Liu, Q. Guan and W. Li, *Catal. Today*, 2019, **330**, 109–116.
2 Z. Chen, X. Li, Y. Xu, Y. Dong, W. Lai, W. Fang and X. Yi, *Catal. Commun.*, 2018, **103**, 1–4.
3 A. Buchholz, W. Wang, M. Xu, A. Arnold and M. Hunger, *Microporous Mesoporous Mater.*, 2002, **56**, 267–278.
4 D. Verma, B. S. Rana, R. Kumar, M. Sibi and A. K. Sinha, *Appl. Catal., A*, 2015, **490**, 108–116.
5 P. Meriaudeau, V. Tuan, V. T. Nghiem, S. Lai, L. Hung and C. Naccache, *J. Catal.*, 1997, **169**, 55–66.
6 Y. Hu, X. Wang, X. Guo, H. Sun and S. Li, *React. Kinet. Catal. Lett.*, 2005, **86**, 45–50.
7 M. Gharibeh, G. A. Tompsett, W. C. Conner and K. S. Yngvesson, *ChemPhysChem*, 2008, **9**, 2580–2591.
8 V. Valtchev and L. Tosheva, *Chem. Rev.*, 2013, **113**, 6734–6760.
9 Q. Liu, H. Zuo, T. Wang, L. Ma and Q. Zhang, *Appl. Catal., A*, 2013, **468**, 68–74.
10 S. R. Venna and M. A. Carreon, *J. Phys. Chem. B*, 2008, **112**, 16261–16265.
11 F. Zhang, Y. Liu, Q. Sun, Z. Dai, H. Gies, Q. Wu, S. Pan, C. Bian, Z. Tian, X. Meng, Y. Zhang, X. Zou, X. Yi, A. Zheng, L. Wang and F.-S. Xiao, *Chem. Commun.*, 2017, **53**, 4942–4945.
12 Y. Liu, W. Qu, W. Chang, S. Pan, Z. Tian, X. Meng, M. Rigutto, A. van der Made, L. Zhao and X. Zheng, *J. Colloid Interface Sci.*, 2014, **418**, 193–199.
13 D. Jin, Z. Liu, J. Zheng, W. Hua, J. Chen, K. Zhu and X. Zhou, *RSC Adv.*, 2016, **6**, 32523–32533.
14 P. Zhang, H. Liu, Y. Yue, H. Zhu and X. Bao, *Fuel Process. Technol.*, 2018, **179**, 72–85.
15 Y. Zhu, Z. Hua, J. Zhou, L. Wang, J. Zhao, Y. Gong, W. Wu, M. Ruan and J. Shi, *Chem.–Eur J.*, 2011, **17**, 14618–14627.
16 L. Yang, S. Xing, H. Sun, C. Miao, M. Li, P. Lv, Z. Wang and Z. Yuan, *Fuel Process. Technol.*, 2019, **187**, 52–62.
17 X. Chen, X. Meng and F.-s. Xiao, *Chin. J. Catal.*, 2015, **36**, 797–800.
18 J. Hua and Y. Han, *Chem. Mater.*, 2009, **21**, 2344–2348.
19 X. He, T. Ge, Z. Hua, J. Zhou, J. Lv, J. Zhou, Z. Liu and J. Shi, *ACS Appl. Mater. Interfaces*, 2016, **8**, 7118–7124.
20 T. Ge, Z. Hua, X. He, J. Lv, H. Chen, L. Zhang, H. Yao, Z. Liu, C. Lin and J. Shi, *Chem.–Eur J.*, 2016, **22**, 7895–7905.
21 J. Sun, Z. Shan, T. Maschmeyer, J. A. Moulijn and M.-O. Coppens, *Chem. Commun.*, 2001, 2670–2671.
22 X. Huang, L. Wang, L. Kong and Q. Li, *Appl. Catal., A*, 2003, **253**, 461–467.
23 A. Sakthivel, S. Dapurkar, N. Gupta, S. Kulshreshtha and P. Selvam, *Microporous Mesoporous Mater.*, 2003, **65**, 177–187.
24 C. Emeis, *J. Catal.*, 1993, **141**, 347–354.
25 P. Meriaudeau, V. A. Tuan, F. Lefebvre, V. T. Nghiem and C. Naccache, *Microporous Mesoporous Mater.*, 1998, **22**, 435–449.
26 J. A. Martens, P. J. Grobet and P. A. Jacobs, *J. Catal.*, 1990, **126**, 299–305.
27 T. Blasco, A. Chica, A. Corma, W. Murphy, J. Agúndez-Rodríguez and J. Pérez-Pariente, *J. Catal.*, 2006, **242**, 153–161.
28 B. Chen and Y. Huang, *J. Phys. Chem. C*, 2007, **111**, 15236–15243.
29 B. Chen and Y. Huang, *Microporous Mesoporous Mater.*, 2011, **143**, 14–21.
30 S. Mintova, N. H. Olson, V. Valtchev and T. Bein, *Science*, 1999, **283**, 958–960.
31 S. R. Challa, A. T. Delariva, T. W. Hansen, S. Helveg, J. Sehested, P. L. Hansen, F. Garzon and A. K. Datye, *J. Am. Chem. Soc.*, 2011, **133**, 20672–20675.
32 K. Fang, J. Ren and Y. Sun, *J. Mol. Catal. A: Chem.*, 2005, **229**, 51–58.

